LETTERS
PUBLISHED ONLINE: 26 JULY 2009 | DOI: 10.1038/NNANO.2009.190
nature nanotechnology

Optical nanocrystallography with tip-enhanced phonon Raman spectroscopy

Samuel Berweger[1], Catalin C. Neacsu[1], Yuanbing Mao[2], Hongjun Zhou[2], Stanislaus S. Wong[2,3] and Markus B. Raschke[1]*

Conventional phonon Raman spectroscopy is a powerful experimental technique for the study of crystalline solids[1–5] that allows crystallography, phase and domain identification[6,7] on length scales down to ~1 μm. Here we demonstrate the extension of tip-enhanced Raman spectroscopy to optical crystallography on the nanoscale by identifying intrinsic ferroelectric domains of individual $BaTiO_3$ nanocrystals through selective probing of different transverse optical phonon modes in the system. The technique is generally applicable for most crystal classes, and for example, structural inhomogeneities, phase transitions, ferroic order and related finite-size effects occurring on nanometre length scales can be studied with simultaneous symmetry selectivity, nanoscale sensitivity and chemical specificity.

Taking advantage of the local field enhancement provided by the nanoscopic apex of a plasmonic scanning probe tip, tip-enhanced Raman spectroscopy (TERS) achieves spatial resolution in the nanometre range. TERS of molecular adsorbates[8] and carbon nanotubes[9] with sensitivity down to the single molecule level[10–12] has been demonstrated. Although previously used in a specific tip-enhanced geometry to maximize the near-field contrast[13,14], the full potential offered by the symmetry selectivity of the Raman response has not yet been explored[15]. Here we derive and experimentally demonstrate the tensor-based phonon Raman selection rules that will enable TERS to determine crystallographic orientation in general, and the ferroelectric order in particular, of crystalline solids, with nanometre spatial resolution.

Without loss of generality we use tetragonal $BaTiO_3$ as a specific example. A variety of potential nanoscale devices are based on the ferroelectric properties of $BaTiO_3$, including piezoelectric actuators and non-volatile memory[16]. In addition, although it has long been considered a prototypical displacive ferroelectric[17], recent experiments have indicated a more complex mechanism with order–disorder contributions[17,18]. This makes a fundamental understanding of its nanoscale ferroelectric order and domain behaviour desirable.

Perovskite $BaTiO_3$ has a paraelectric pseudocubic phase above a Curie temperature of $T_C = 120\,^{\circ}C$. Below T_C its non-centrosymmetric tetragonal $4mm$ phase is characterized by the intrinsic formation of ferroelectric domains polarized along the crystallographic c-axis. In keeping with conventional definitions, domains formed parallel to the length of the rod are referred to as c-domains (see Fig. 1), and those perpendicular as $a_{x'}$- and $a_{y'}$-domains, that is, oriented in the sample plane and along the surface normal, respectively.

Figure 2a shows a TERS spectrum acquired for 60 s on top of a $BaTiO_3$ nanorod (unpolarized detection, oblique rod orientation). The two dominant peaks can be assigned to the A_1 transverse optical (TO) mode at 516 cm^{-1}, the E longitudinal optical (LO) mode at 715 cm^{-1}, and the spectrally unresolved A_1 LO and E TO modes at 727 cm^{-1} and 487 cm^{-1}, respectively[19]. The Raman-active LO modes are characteristic of the tetragonal phase[20], and their observation thus reflects the ferroelectric state. A tip–sample distance dependence of the Raman response is shown in Fig. 2b, with spectra acquired for 10 s each. For the tip within 30 nm of the nanorod and correlated with the apex radius, a rise in the near-field signal above the far-field response is seen. A lateral line scan exhibiting the enhanced Raman signal across a $BaTiO_3$ nanorod is shown in Fig. 2c, together with the corresponding topography. Changes in the LO peak intensity across the rod can be attributed to fluctuations in the near-field k-vector distribution from the tip near the edges of the rod. The underlying Raman tip enhancement $I \approx 10^4 - 10^5$ can be derived from the distance dependence and lateral scan (see Supplementary Information).

These results demonstrate the capability of TERS for imaging crystalline nanostructures based on the optical phonon response. With the Raman tensor reflecting the crystal symmetry, selective probing of specific phonon modes in certain scattering geometries then allows for determination of the crystal orientation and associated ferroelectric order. Specifically, the induced Raman polarization of the optical phonon mode n is given by $P^{rad}_{i,n} \propto \mathcal{F}_{ij}\chi_{jk,n}\mathcal{F}'_{kl}E^{inc}_l$ $(i,j,k,l = x,y,z)$ with Raman tensor $\chi_{jk,n}$, incident light E^{inc}_l, and tip scattering tensors $\mathcal{F}_{ij}$ and $\mathcal{F}'_{kl}$ reflecting the TERS geometry. For polar phonon modes the relationship between the phonon polarization direction, the phonon wavevector $\boldsymbol{q}$, and its momentum conservation with incident and scattered wavevector ($\boldsymbol{q} = \boldsymbol{k}_i - \boldsymbol{k}_s$) then dictates the excitation of the spectrally distinct LO and TO A_1 and E modes.

In TERS these fundamental Raman selection rules are superimposed by the additional considerations of the polarization-selective enhancement and scattering by the tip of both incident radiation and induced Raman polarization, due to both the optical antenna geometry and excitation of an axial plasmon resonance[13]. This can be expressed by the effective (empirical) scattering tensors $\mathcal{F}_{ij}$ and $\mathcal{F}'_{kl}$, describing the spatial anisotropy in tip scattering efficiency and local field enhancement, respectively, associated with the broken symmetry of the tip in its axial direction (∞mm symmetry). In general, with $F_p \simeq F'_p > F_s \simeq F'_s$ for the tensor elements (with s and p referring to the polarization direction of Raman scattered and incident light, as shown in Fig. 1a) the details of which depend on the nature of the tip plasmon excitation, the amount of Raman shift or the degree of depolarization due to tip inhomogeneities[21–23] (see Supplementary Information).

To determine the ferroelectric order in $BaTiO_3$ we considered a nanorod oriented parallel to the incident light as shown in Fig. 1. From the symmetry of the Raman tensor (see Supplementary

[1]Department of Chemistry and Department of Physics, University of Washington, Seattle, Washington 98195, USA, [2]Department of Chemistry, State University of New York at Stony Brook, Stony Brook, New York 11794-3400, USA, [3]Condensed Matter and Material Sciences Department, Brookhaven National Laboratory, Upton, New York 11973, USA. *e-mail: raschke@chem.washington.edu

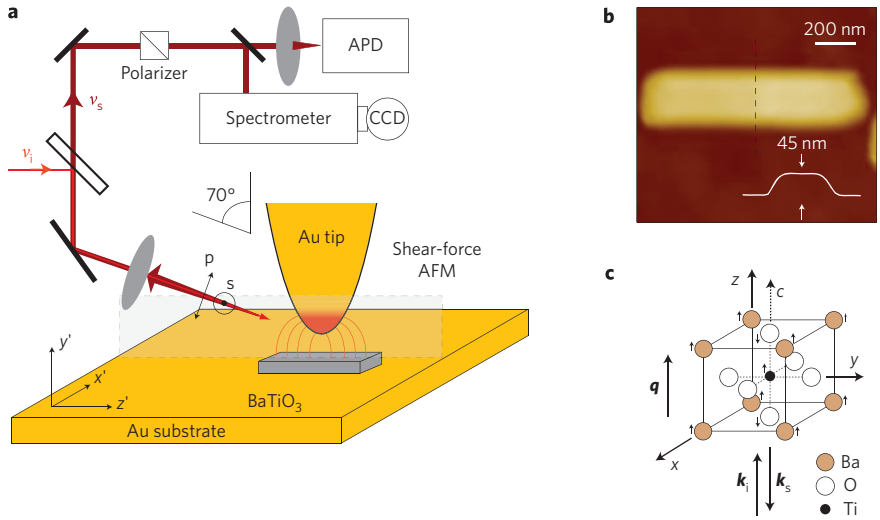

Figure 1 | Experimental setup and crystal symmetry. a, Schematic of the experimental TERS setup for backscattering Raman imaging of nanocrystals based on phonon Raman selection rules (see Methods). **b**, Shear-force topography of a typical $BaTiO_3$ nanorod with a height of ~45 nm. **c**, Ferroelectric displacement (*c*-domain) and geometry illustrating the phonon Raman excitation process with optical wavevectors ($\boldsymbol{k}_i$, $\boldsymbol{k}_s$) and phonon wavevector $\boldsymbol{q}$. The coordinates x', y', z' and x, y, z refer to the laboratory and sample frame, respectively.

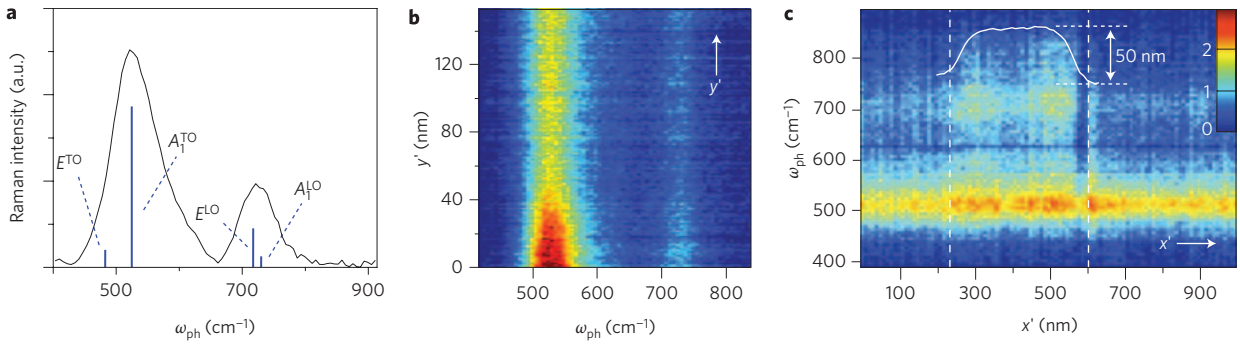

Figure 2 | Phonon TERS of $BaTiO_3$. a, TERS spectrum acquired on a $BaTiO_3$ nanorod with phonon mode assignment (fluorescence background subtracted). **b**, Corresponding tip–sample distance dependence. **c**, Spectrally resolved line scan across a $BaTiO_3$ nanorod. (The abrupt signal change at $x' = 580$ nm is due to an acquisition artifact).

Information) it follows that probing the *c*-domain in the absence of a polarization contribution along the *z*-axis, the *E* modes do not contribute to the Raman signal. In contrast, for the $a_{x'}$- and $a_{y'}$-domain configurations, with either the incident or scattered light polarized along the respective ferroelectric polarization directions, both $E(x)$ and $E(y)$ TO modes contribute. The A_1 mode may be observed in all domain orientations, as the diagonal A_1 tensor allows the strongly enhanced $p_{in}p_{out}$ combination for all cases. Specifically, for the *c*- and *a*-domains, as a result of the phonon propagating parallel or perpendicular with respect to the phonon polarization direction, either the A_1 LO or A_1 TO mode is excited, respectively. With the A_1 TO mode being strongest, followed by the *E* TO mode, this provides the imaging contrast to distinguish the *c*- and *a*-domains in the experiment.

Owing to the limited signal-to-noise ratio resulting in impractically long scan times (sample drift), we performed spectrally integrated detection for sample scanning. The associated overall *E* LO and A_1 TO Raman signal intensity variations as dictated by the selection rules provided the contrast between the different ferroelectric domains. Figure 3 shows the shear-force topography (Fig. 3a) of an individual $BaTiO_3$ nanorod on a gold substrate together with the TERS signal acquired for 10 ms per pixel with incident *p*-polarization (Fig. 3b). In the TERS image a region of ~60 nm × 400 nm associated with an enhanced near-field Raman signal can be discerned. The overall signal trend across the domain can be attributed to variations in the far-field illumination conditions of the tip apex due to the rod being scanned under the tip, as is evident from the concurrent spatial fluorescence variations of the gold surface adjacent to the rod. Under the given nanorod orientation and TERS geometry a low signal intensity for the *c*-domain is expected due to the weak A_1 LO mode and the absence of the *E* mode, in contrast to a larger signal for the *a*-domains arising predominantly from the strong A_1 TO mode. Under the backscattering geometry, a further spectroscopic distinction of the *a*-domain into $a_{x'}$ and $a_{y'}$ is not readily possible, as this would manifest itself only in a difference in the respective A_1 TO Raman amplitudes. However, with the domain boundaries known to be oriented 45° with respect to the domain orientations[24], the observation of the surface domain boundary parallel to *z* suggests an $a_{y'}$-domain. This allows for the domain assignment as shown in Fig. 3d.

This assignment is corroborated by the cross-section profiles for the topography and TERS signal shown in Fig. 3c. At the left domain boundary the TERS contrast coincides with a ~3 nm topographic height variation. Related topographic features in single-crystal bulk $BaTiO_3$ associated with ferroelectric domain boundaries have been observed previously[25,26].

The localized regions of strong optical signal on the gold substrate itself, as seen in Fig. 3, are due to nanometre-scale height

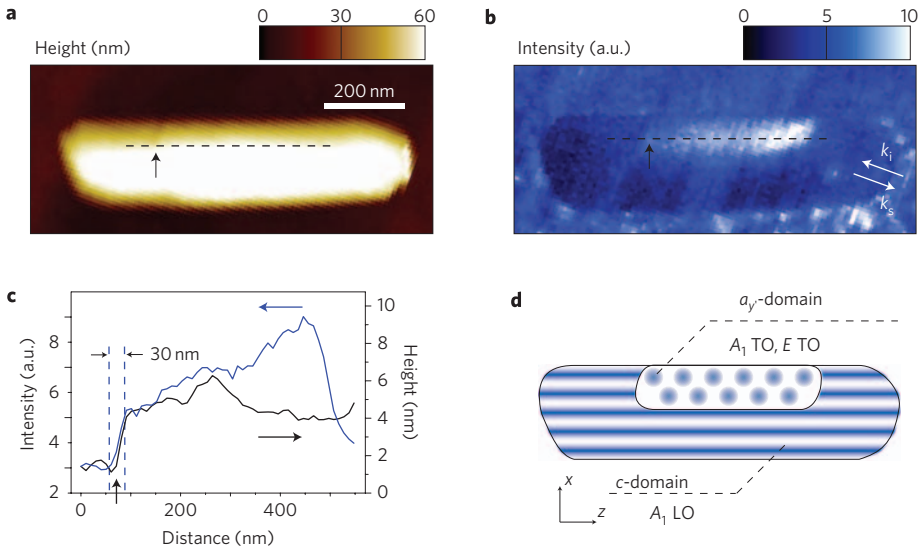

Figure 3 | Spatially resolved TERS for ferroelectric domain imaging. a, Topography of a $BaTiO_3$ nanorod. **b**, The spectrally integrated TERS signal for ferroelectric domain imaging. **c**, Lateral cross-section along the dashed lines in **a** and **b** of the region of high TERS signal (blue) and corresponding topography (black) on the rod. **d**, Domain assignment based on the Raman selection rules for the TERS geometry used.

variations inherent to the evaporated gold substrate that lead to an increase and associated spatial variation in the intrinsic tip-fluoresence contributing to the signal background[27]. Conversely, the apparent overall signal decrease with the tip positioned above the *c*-domain of the $BaTiO_3$ is due to the weak near-field Raman response from the A_1 LO mode and the decrease in tip-enhanced fluorescence background. However, despite the short range of the evanescent tip–sample coupling the TERS process nevertheless benefits from the Fresnel factors of the Au substrate providing additional far-field enhancement.

Previously, the use of birefringence in the infrared spectral range has allowed for near-field imaging of ferroelectric domains in bulk $BaTiO_3$ (ref. 28). Similarly, piezoelectric force microscopy can identify ferroelectric domains. However, with its ability to probe multiple tensors simultaneously, phonon Raman scattering using TERS provides an enhanced versatility, allowing crystal symmetry properties to be probed in addition to its *a priori* capability of determining the chemical identity and structural phase of the material.

The power of the symmetry sensitivity of the Raman response becomes particularly evident when considering that the lattice constants differ between the cubic paraelectric phase and the tetragonal ferroelectric phase by only 0.044 Å, making their distinction difficult even with high-resolution transmission electron microscopy in combination with electron diffraction techniques[29,30].

Ferroelectric domains arise from an interplay between the depolarization energy lowered by the formation of domains and the increased energy associated with domain walls[24]. Our results show that, despite crystal sizes of only several hundreds of nanometres, and as such comparable to or smaller than typical domains found for bulk dielectrics, these nanocrystals are not necessarily single domain. Although *a*-domains have previously been artificially induced in chemically synthesized $BaTiO_3$ nanorods[30], our study provides evidence of spontaneous domain formation in such structures. This may indicate finite size effects on ferroelectric ordering due to the large surface-to-volume ratio by, for example, pinning due to surface defects, the possible influence of adsorbates, and the influence of the surface free energy in general and its spatial variation with crystal shape and size.

Methods

A TERS setup based on a scattering-type scanning near-field optical microscope (*s*-SNOM) was used, as shown schematically in Fig. 1a. Side-on tip illumination with near–grazing angle (70°) was provided by a HeNe laser ($\lambda = 632.8$ nm), with a maximum fluence of $\sim 2.1 \times 10^4$ W cm^{-2} at the focus of a long working distance microscope objective (Nikon, NA = 0.35, working distance = 20.5 mm). Electrochemically etched gold tips with tip radii of ~10–20 nm were used as described previously[31], and were mounted on the quartz tuning fork of a shear-force atomic force microscope (AFM). The optical signal was spectrally filtered with a notch filter (cutoff ≈ 400 cm^{-1}) and detected using either an avalanche photodiode (APD), or spectrally resolved using an imaging spectrograph coupled to a N_2(l)-cooled charge-coupled device (CCD) (Acton Research SpectraPro 500i). The spectral resolution (slit width) of the imaging spectrograph was set to ~40 cm^{-1} to maximize the signal-to-noise ratio while still maintaining the capability to distinguish the TO and LO modes.

The $BaTiO_3$ nanocrystals were synthesized using a molten salt process. BaC_2O_4 was mixed with TiO_2, NaCl and a nonionic surfactant, and heated to 820 °C for 3.5 h as described in ref. 29. The resulting single crystalline $BaTiO_3$ nanorods were characterized by transmission electron microscopy and dispersed onto an evaporated gold substrate by spin coating from ethanol. Figure 1b shows the shear-force atomic force microscopy topography of a $BaTiO_3$ nanocrystal with typical dimensions of ~1.4 μm × 200 nm × 45 nm.

Received 24 December 2008; accepted 19 June 2009; published online 26 July 2009

References

1. Cardona, M. (ed.) *Light Scattering in Solids I* (Springer, 1983).
2. Bustarret, E. *et al.* Superconductivity in doped cubic silicon. *Nature* **444,** 465–468 (2006).
3. Fleury, P. A. & Worlock, J. M. Electric-field-induced Raman scattering in $SrTiO_3$ and $KTaO_3$. *Phys. Rev.* **174,** 613–623 (1968).
4. Leite, R. C. C., Scott, J. F. & Damen, T. C. Multiple-phonon resonant raman scattering in CdS. *Phys. Rev. Lett.* **22,** 780–782 (1969).
5. Cerdeira, F., Buchenauer, C. J., Pollak, F. H. & Cardona, M. Stress-induced shifts of first-order Raman frequencies of diamond- and zinc-blende-type semiconductors. *Phys. Rev. B* **5,** 580–593 (1972).
6. Deluca, M., Higashino, M. & Pezzotti, G. Raman tensor elements for tetragonal $BaTiO_3$ and their use for in-plane domain texture assessments. *Appl. Phys. Lett.* **91,** 091906 (2007).
7. Lagos, P. L. *et al.* Identification of ferroelectric domain structure in $BaTiO_3$ for Raman spectroscopy. *Surf. Sci.* **532,** 493–500 (2003).
8. Bailo, E. & Deckert, V. Tip-enhanced raman spectroscopy of single RNA strands: towards a novel direct-sequencing method. *Angew. Chem. Int. Ed.* **47,** 1658–1661 (2008).
9. Hartschuh, A., Sánchez, E. J., Xie, X. S. & Novotny, L. High-resolution near-field Raman microscopy of single-walled carbon nanotubes. *Phys. Rev. Lett.* **90,** 095503 (2003).
10. Neacsu, C. C., Dreyer, J., Behr, N. & Raschke, M. B. Scanning-probe Raman spectroscopy with single-molecule sensitivity. *Phys. Rev. B* **73,** 193406 (2006).
11. Zhang, W., Yeo, B. S., Schmid, T. & Zenobi, R. Single molecule tip-enhanced Raman spectroscopy with silver tips. *J. Phys. Chem. C* **111,** 1733–1738 (2007).

12. Steidtner, J. & Pettinger, B. Tip-enhanced Raman spectroscopy and microscopy on single dye molecule with 15 nm resolution. *Phys. Rev. Lett.* **100,** 236101 (2008).
13. Ossikovski, R., Nguyen, Q. & Picardi, G. Simple model for the polarization effects in tip-enhanced Raman spectroscopy. *Phys. Rev. B* **75,** 045412 (2007).
14. Motahashi, M., Hayazawa, N., Tarun, A. & Kawata, S. Depolarization effect in reflection-mode tip-enhanced Raman scattering for Raman active crystals. *J. Appl. Phys.* **103,** 034309 (2008).
15. Matsui, R., Verma, P., Ichimura, T., Inouye, Y. & Kawata, S. Nanoanalysis of crystalline properties of GaN thin film using tip-enhanced Raman spectroscopy. *Appl. Phys. Lett.* **90,** 061906 (2007).
16. Setter, N. *et al.* Ferroelectric thin films: review of materials, properties and applications. *J. Appl. Phys.* **100,** 051606 (2006).
17. Zalar, B., Laguta, V. V. & Blinc, R. NMR evidence for the coexistence of order-disorder and displacive components in barium titanate. *Phys. Rev. Lett.* **90,** 037601 (2003).
18. Maksimov, E. G., Matsko, N. L., Ebert, S. V. & Magnitskaya, M. V. Some problems in the theory of perovskite ferroelectrics. *Ferroelectrics* **354,** 19–38 (2007).
19. Jang, M.-S., Takashige, M., Kojima, S. & Nakamura, T. Oblique phonons with special concern to the soft phonon mode in tetragonal $BaTiO_3$. *J. Phys. Soc. Jpn* **52,** 1025–1033 (1983).
20. Perry, C. H. & Hall, D. B. Temperature dependence of the Raman spectrum of $BaTiO_3$. *Phys. Rev. Lett.* **15,** 700–702 (1965).
21. Neacsu, C. C., Steudle, G. A. & Raschke, M. B. Plasmonic light scattering from nanoscopic metal tips. *Appl. Phys. B* **80,** 295–300 (2005).
22. Le Ru, E. C. *et al.* Experimental verification of the SERS electromagnetic model beyond the $|E|^4$ approximation: polarization effects. *J. Phys. Chem. C* **112,** 8117–8121 (2008).
23. Gucciardi, P. G. *et al.* Light depolarization induced by metallic tips in apertureless near-field optical microscopy and tip-enhanced Raman spectroscopy. *Nanotechnology* **19,** 215702 (2008).
24. Lines, M. & Glass, A. *Principles and Applications of Ferroelectric and Related Materials* (Oxford Univ. Press, 2001).
25. Munoz-Saldana, J., Schneider, G. A. & Eng, L. M. Stress induced movement of ferroelastic domain walls in $BaTiO_3$ single crystals evaluated by scanning force microscopy. *Surf. Sci.* **480,** L402–L410 (2001).
26. Kalinin, S. V. & Bonnell, D. A. Effect of phase transition on the surface potential of the $BaTiO_3$ (100) surface by variable temperature scanning surface potential microscopy. *J. Appl. Phys.* **87,** 3950–3957 (2000).
27. Sackrow, M., Stanciu, C., Lieb, M. A. & Meixner, A. J. Imaging nanometer-sized hot spots on smooth Au films with high-resolution tip-enhanced luminescence and Raman near-field optical microscopy. *Chem Phys Chem* **9,** 316–320 (2008).
28. Kehr, S. C. *et al.* Anisotropy contrast in phonon-enhanced apertureless near-field microscopy using a free-electron laser. *Phys. Rev. Lett.* **100,** 256403 (2008).
29. Mao, Y., Banerjee, S. & Wong, S. S. Large-scale synthesis of single-crystalline perovskite nanostructures. *J. Am. Chem. Soc.* **125,** 15718–15719 (2003).
30. Yun, W. S., Urban, J. J., Gu, Q. & Park, H. Ferroelectric properties of individual barium titanate nanowire investigated by scanned probe microscopy. *Nano Lett.* **2,** 447–450 (2002).
31. Ren, B., Picardi, G. & Pettinger, B. Preparation of gold tips suitable for tip-enhanced Raman spectroscopy and light emission by electrochemical etching. *Rev. Sci. Instrum.* **75,** 837–841 (2004).

Acknowledgements

S. Berweger acknowledges support from the University of Washington Center for Nanotechnology with funding from NSF-IGERT. Funding from the National Science Foundation (NSF CAREER grant CHE 0748226) is gratefully acknowledged.

Author contributions

S.B., C.C.N., and M.B.R. conceived the experiments. S.B. and C.C.N. carried out the experiments. S.B. performed the data analysis. Y.M., H.Z. and S.S.W. synthesized the sample materials. S.B. wrote the manuscript with contributions from C.C.N. and M.B.R.

Additional information

Supplementary information accompanies this paper at www.nature.com/naturenanotechnology. Reprints and permission information is available online at http://npg.nature.com/reprintsandpermissions/. Correspondence and requests for materials should be addressed to M.B.R.